

UCSF

UC San Francisco Previously Published Works

Title

Dynamic hyperpolarized carbon-13 MR metabolic imaging of nonhuman primate brain

Permalink

<https://escholarship.org/uc/item/3pw4w7k5>

Journal

Magnetic Resonance in Medicine, 71(1)

ISSN

0740-3194

Authors

Park, Ilwoo

Larson, Peder EZ

Tropp, James L

et al.

Publication Date

2014

DOI

10.1002/mrm.25003

Peer reviewed

Published in final edited form as:

Magn Reson Med. 2014 January ; 71(1): 19–25. doi:10.1002/mrm.25003.

Dynamic Hyperpolarized Carbon-13 MR Metabolic Imaging of Nonhuman Primate Brain

Ilwoo Park^{1,*}, Peder E. Z. Larson¹, James L. Tropp², Lucas Carvajal¹, Galen Reed¹, Robert Bok¹, Fraser Robb², John Bringas³, Adrian Kells³, Philip Pivrotto³, Krystof Bankiewicz³, Daniel B. Vigneron¹, and Sarah J. Nelson^{1,4}

¹Surbeck Laboratory of Advanced Imaging, Department of Radiology and Biomedical Imaging, University of California, San Francisco, California, USA

²Global Applied Science Lab, GE Healthcare, Menlo Park, California, USA

³Department of Neurosurgery, University of California, San Francisco, California, USA

⁴Department of Bioengineering and Therapeutic Sciences, University of California, San Francisco, California, USA

Abstract

Purpose—To investigate hyperpolarized ¹³C metabolic imaging methods in the primate brain that can be translated into future clinical trials for patients with brain cancer.

Methods—¹³C coils and pulse sequences designed for use in humans were tested in phantoms. Dynamic ¹³C data were obtained from a healthy cynomolgus monkey brain using the optimized ¹³C coils and pulse sequences. The metabolite kinetics were estimated from two-dimensional localized ¹³C dynamic imaging data from the nonhuman primate brain.

Results—Pyruvate and lactate signal were observed in both the brain and the surrounding tissues with the maximum signal-to-noise ratio of 218 and 29 for pyruvate and lactate, respectively. Apparent rate constants for the conversion of pyruvate to lactate and the ratio of lactate to pyruvate showed a difference between brain and surrounding tissues.

Conclusion—The feasibility of using hyperpolarized [1-¹³C]-pyruvate for assessing in vivo metabolism in a healthy nonhuman primate brain was demonstrated using a hyperpolarized ¹³C imaging experimental setup designed for studying patients with brain tumors. The kinetics of the metabolite conversion suggests that this approach may be useful in future studies of human neuropathology.

Keywords

Hyperpolarized carbon-13 magnetic resonance spectroscopic imaging; dynamic nuclear polarization; pyruvate; primate brain

INTRODUCTION

Dynamic nuclear polarization (DNP) in conjunction with ^{13}C MR metabolic imaging offers an exciting method of assessing in vivo metabolism with a substantial gain in sensitivity over conventional MR methods (1–5). Recent studies using hyperpolarized [1- ^{13}C]-pyruvate as a substrate have demonstrated utility for examining in vivo tumor metabolism in rodent brain tumor models (6–8). These preclinical studies have shown the feasibility of using this technique for differentiation of tumor from normal brain tissue, characterization of ^{13}C metabolite patterns between pathologically heterogeneous abnormal and normal brain tissue, and detection of early response to treatment in animal models of high-grade gliomas.

The first clinical trial using hyperpolarized ^{13}C MR metabolic imaging has been successfully performed in patients with prostate cancer (9). This study showed that there were no dose limiting toxicities following an injection of hyperpolarized [1- ^{13}C]-pyruvate and demonstrated the feasibility of using this technique for evaluating hyperpolarized pyruvate and its metabolic products in humans.

Although previous studies have shown the potential of applying DNP technology to brain cancer using rodent models (6–8), animal experiments with a larger brain size and an anatomy similar to human brain would be beneficial in translating this technique to a clinical trial for patients with brain tumor. The purpose of this study was to design a strategy for obtaining hyperpolarized ^{13}C metabolic imaging from patients with brain cancer and to demonstrate its feasibility by acquiring data from a preclinical primate model. ^{13}C coils and pulse sequences were first tested in phantoms. Dynamic ^{13}C data were then obtained from a healthy nonhuman primate brain using the optimized ^{13}C coils and pulse sequences, and metabolic kinetics were estimated.

METHODS

All experiments were performed using a 3T clinical MRI system (GE Healthcare, Waukesha, Wisconsin, USA) with 40 mT/m, 150 mT/m/ms gradients, a broadband radiofrequency (RF) amplifier, and a multinuclear spectroscopy hardware package. Two ^{13}C RF coil configurations were developed in-house (Fig. 1): a volume transmit-receive birdcage ^{13}C coil with an inner diameter of 28 cm (Fig. 1a) and a bore-insertable volumetric ^{13}C transmit coil with a clamshell hinge for ease of patient loading (10) and a bilateral eight-channel phased array receive coil (11,12) (Fig. 1b and 1c). The bilateral eight-channel phased array receive coil consists of two curved panels, with each panel containing a linear arrangement of four coil elements.

In order to assess and compare the performance of two coils, a human head-shaped phantom containing ethylene glycol ($\text{HOCH}_2\text{CH}_2\text{OH}$, anhydrous, 99.8%, Sigma-Aldrich, St. Louis, Missouri, USA) was scanned using the birdcage and clamshell/phased array coil configurations (Fig. 2a). The phantom had the size of a human head with the following dimensions: right–left = 15 cm, anterior–posterior = 18 cm, superior–inferior = 22 cm. For the scan with the clamshell/phased array coils, the distance between the centers of the two receive coils was 17 cm. ^{13}C spectral data were acquired from a slice with a thickness of 1,

2, 3, and 4 cm using a ^{13}C two-dimensional (2D) MR spectroscopic imaging sequence (echo time/pulse repetition time = 3/3,000 ms, 5 kHz sweep width, 2,048 spectral points) (6). A 20×20 matrix size with the field of view (FOV) of 20 cm produced voxel sizes of 1, 2, 3 and 4 cc.

A 9-year-old female cynomolgus monkey (*macaca fascicularis*, body weight = 4.3 kg) was studied on two occasions to verify the developed experimental setup for human brain study. Before each imaging experiment, the animal was intubated, placed on a heated pad, and administered inhaled isoflurane anesthesia (1%–3%). A catheter was placed in the saphenous vein for intravenous administration of the hyperpolarized pyruvate solution. The animal was transferred to the MR scanner and placed on a circulating water blanket in the supine position. Anesthesia was maintained with a constant delivery of isoflurane (1%–3%), and vital signs were monitored using pulse oximetry. Foam pads were used to stabilize the animal's head within the RF coil. For the acquisition using clamshell/phased array coils, the distance between the centers of the two receive panels was 14 cm. All protocols were approved and followed procedures specified by the University of California, San Francisco Institutional Animal Care and Use Committee.

Prior to each ^{13}C imaging experiment, T_1 -weighted anatomical images were obtained in the axial and sagittal planes using an inversion recovery spoiled gradient echo (IRSPGR) sequence (echo time/repetition time/inversion time = 2.5/8.4/400 ms, 25 cm FOV, 256×256 matrix, 3 mm slice thickness, and 5 NEX) from the body coil.

The hyperpolarized [$1\text{-}^{13}\text{C}$]-pyruvate was produced using either a prototype SpinLab (General Electric, Niskayuna, New York, USA) (13) or a HyperSense (Oxford Instruments, Abingdon, UK) DNP polarizer. For the SpinLab system, a mixture consisting of 1,000 μL (~1,280 mg) of $\text{C}1$ -labeled pyruvic acid and 15 mM trityl radical was polarized. For the HyperSense system, a mixture of 200 μL (~260 mg) $\text{C}1$ -labeled pyruvic acid and 15 mM trityl radical was used. After ~1.5 hours of microwave irradiation, the hyperpolarized pyruvic acid was rapidly dissolved in an aqueous solution with 40 mM Tris, 100 mM NaOH, and 0.3 mM Na_2 ethylenediaminetetraacetic acid. The hyperpolarized solution was then transferred to the magnet for ^{13}C imaging, and an aliquot of the pyruvate solution was used to measure the liquid-state polarization using a custom-built low-field NMR spectrometer. The final dissolved solution had a concentration of 250 mM (0.38 mmol/kg) pyruvate and pH of 7.5 ± 0.3 .

The following ^{13}C dynamic spectroscopic data were acquired from a 20-mm slice through the brain: slice-localized data with 10° flip angle (echo time/pulse repetition time = 35/3,000 ms, 3 s temporal resolution, 64 total time points), 2D-localized data with a multiband RF excitation using $20^\circ/4^\circ$ for lactate/pyruvate flip angle (echo time/pulse repetition time = 4.6/130 ms, 3 s temporal resolution, 24 total time points) (14) and 2D-localized data with a variable flip angle multiband RF excitation (echo time/pulse repetition time = 6.1/130 ms, 3 s temporal resolution, 10 total time points) (15,16). The 2D-localized data had 10 phase encodes in the anterior–posterior direction and a symmetric echo-planar readout in the right–left direction, providing 10×10 mm in-plane resolution. Slice-localized and 2D-localized data were acquired during or following a 5 s injection of ~6.1 mL [$1\text{-}^{13}\text{C}$]-pyruvate (250

mM, 0.38 mmol/kg) through the saphenous vein. Table 1 shows a summary of nonhuman primate studies.

The ^{13}C 2D MR spectroscopic imaging data from the phantom were processed with software developed in our laboratory (17). For the data from the clamshell/phased array coil configuration, the individual spectra were added as the square root of the sum of the square with an equal weight for all channels. The signal-to-noise ratios (SNR) were calculated as the magnitude peak height over the standard deviation (SD) of the first 200 points of the spectra in a region that contained no signal. The spatial variation of signal across the phantom was compared between the birdcage and clamshell/phased array coils for different voxel sizes. The slice-localized ^{13}C dynamic data were processed with MATLAB 7.0 (Mathworks Inc., Natick, Massachusetts, USA). Individual FIDs were apodized with a 10-Hz Lorentzian filter in the time domain and Fourier-transformed to produce ^{13}C spectra at each time point. The 2D-localized ^{13}C dynamic data were processed using MATLAB scripts developed in our laboratory (17). The k-space FIDs were apodized by a 10-Hz Gaussian filter in the time domain and zero-filled to 256 points. The data were then Fourier-transformed to produce a 3D spatial and temporal array. An additional linear phase correction was applied in the symmetric echo-planar dimension to correct for the offset of individual k-space points (14). For the 2D-localized dynamic data that were acquired using variable flip angle excitation, the lactate and pyruvate signals were corrected for the differential flip angle, and apparent rate constants for the conversion of pyruvate to lactate (K_{PL}) were estimated using a two-site exchange model (18) for voxels where the maximum SNR of pyruvate were >40 .

RESULTS

The spatially dependent SNR characteristics of the two coils used for this study is shown in Figure 2. The SNRs from a row of spectra in the middle of the phantom were plotted against the relative location in right-left direction for each coil (Fig. 2c and 2d). The birdcage coil produced a relatively uniform signal across the phantom and its SNR increased linearly with an increase in voxel volume (Fig. 2c). The mean SNR in the center 4 voxels from the birdcage coil was 10.6, 20.8, 30.4, and 39.4 for 1, 2, 3, and 4 cc voxels, respectively (Table 2). The signal from the clamshell/phased array coils appeared to be highest in the voxels closest to the paddle array and dropped as the distance from the coil increased (Fig. 2d). The mean SNR in the center 4 voxels from the clam-shell/phased array coils was 13.1, 25.7, 39.2, and 50.8 for 1, 2, 3, and 4 cc voxel, respectively (Table 2), which was an average of 26% higher than the birdcage coil. The maximum SNR near the coils was 4 to 5 times higher than the mean SNR in the middle for the clam-shell/phased array coil setup.

The use of hyperpolarized [$1\text{-}^{13}\text{C}$]-pyruvate provided sufficient signal to detect the transfer of ^{13}C label to lactate in nonhuman primate brain. Figure 3 shows slab-localized ^{13}C dynamic data from a 20 mm slice of brain. Figure 3a shows a sagittal image illustrating the slice coverage of the hyperpolarized ^{13}C dynamic data acquisition. Figure 3d shows representative ^{13}C dynamic spectra from the ^{13}C clamshell/phased array coils. Each horizontal line corresponds to a summed magnitude spectrum acquired at a time resolution of 3 s. The SNR of pyruvate and lactate were plotted as a function of time for birdcage (Fig.

3b) and clamshell/phased array (Fig. 3c) coils. The pyruvate signal (173 ppm) reached a maximum at ~12 s after the start of the pyruvate injection, while the lactate signal maximum (185 ppm) was at ~24 seconds. The lactate signal maintained a relatively constant level for 12–15 s at the maximum value. The pyruvate signal decreased rapidly from the maximum peak, and the lactate signal decreased at a slightly slower rate than the pyruvate. $[1-^{13}\text{C}]$ -pyruvate–hydrate was also observed between pyruvate and lactate resonances, but had relatively low signal amplitude (Fig. 3d).

The 2D-localized ^{13}C dynamic spectroscopic imaging from the brain of the nonhuman primate allowed for the temporally and spatially resolved imaging of pyruvate and lactate. Figure 4a and 4b shows a pyruvate signal map over time from the 2D-localized data acquired with the $20^\circ/4^\circ$ lactate/pyruvate flip angle scheme using the birdcage and clamshell/phased array coils, respectively. The pyruvate signal appeared throughout the brain and quickly reached its maximum at 9 s from the end of pyruvate injection. The maximum pyruvate SNR was 67 and 218 for the birdcage and clamshell/phased array coil, respectively. Figure 4c–4e illustrates the data from the 2D-localized data acquired with the variable flip angle scheme using the clamshell/phased array coils. The maximum SNR of pyruvate and lactate were 177 and 29, respectively. The pyruvate signal in the brain reached its maximum at 9 s from the end of injection, and the lactate signal at 30 s (Fig. 4c). When corrected for the variable flip angle, the maximum lactate appeared at 18 s (Fig. 5). A representative axial image and the corresponding magnitude spectra acquired at 30 s with the clamshell/phased array coils are illustrated in Figure 4d. Both pyruvate (blue arrow) and lactate peak (red arrow) were detected in brain as well as surrounding tissue.

Figure 5 shows the overlay image of apparent rate constants for the conversion of pyruvate to lactate and examples of time courses of pyruvate and lactate with the corresponding curve fits from the data acquired with the variable flip angle scheme using the clamshell/phased array coils (exam 2c in Table 1). The pyruvate and lactate signals were corrected for the variable flip angles. K_{PL} was $0.0026 \pm 0.0004 \text{ s}^{-1}$ (mean \pm SD, $n = 13$) for the voxels within the brain (Fig. 5b) and $0.0042 \pm 0.001 \text{ s}^{-1}$ (mean \pm SD, $n = 18$) for the voxels surrounding the brain (Fig. 5c), which included brain tissue, muscle, and vasculature. The mean standard error estimated from the covariance matrix of the model fitting was 0.0007 s^{-1} for the voxels within the brain and 0.001 s^{-1} for the voxels surrounding the brain.

DISCUSSION

In this study, we established a hyperpolarized ^{13}C metabolic imaging method designed for application to human brain. The proposed pulse sequences and ^{13}C coils were tested using a phantom with the size of a human head and a nonhuman primate brain. Nonhuman primate was a good fit for this study because its brain is large and has a structure similar to human brain. To our knowledge, this study demonstrated for the first time the use of hyperpolarized ^{13}C imaging to study in vivo brain metabolism in a primate brain. Excellent pyruvate and lactate signal were observed in the primate brain as well as its surrounding tissue.

The SpinLab is a new polarizer design with specifications that are focused on clinical use with a large volume of substrate polarization and dissolution process. Our study was the first to use the SpinLab system for animals larger than rodents. One of the reasons for using the two polarizers in this study was to establish the feasibility of using the SpinLab by comparing with the more well-established HyperSense system. Both systems were able to generate hyperpolarized pyruvate solutions. One of the polarization measurements had a relatively low level of polarization (Table 1). We believe that air bubbles in the syringe that contained the aliquot of pyruvate solution for polarization measurement caused the low polarization level. A proper degassing of the pyruvate solution in the syringe was applied in the subsequent polarization measurements. On average, the SpinLab system produced a 50% higher polarization than the Hyper-Sense system (Table 1). This increase was due to the lower sample vial temperature in the SpinLab system (~1 K) compared with the HyperSense system (1.2 K) (19). The ability to produce the higher level of polarization and larger volumes for rapid, successive injections makes the SpinLab system a promising tool to probe ^{13}C metabolism in future preclinical and clinical studies.

The birdcage and clamshell/phased array coils displayed a distribution of signal across the phantom with the size of human head. The birdcage coil rendered relatively uniform signal across the phantom. In comparison to the birdcage coil, the clamshell/phased array setup produced on average 26% higher signal in the middle of the phantom (Table 2). The clamshell/phased array coils produced on average 179% higher signal in the region close to the receive coil surface compared with the region in the middle. Two linear panels in the phased array coils contain the linear arrangement of four surface coils (Fig. 1b), which contributed to a decrease in signal toward the center of the phantom. One should be careful to avoid the misinterpretation of metabolite signal intensity because it depends on the relative location of the voxel to the coils. One way to overcome this issue is to use the apparent rate constant for pyruvate to lactate conversion (Fig. 5) or the ratio of lactate to pyruvate (Fig. 4e) for quantification.

Previously, we successfully acquired 2D dynamic data with an echo planar readout gradient (14), and established the feasibility of this method for acquiring human data from prostate cancer patients (9). However, The majority of previous experiments using 2D dynamic imaging were performed with a fixed flip angle method. The use of a variable flip angle has been proposed as a method to preserve the pyruvate and lactate magnetization for a longer period and hence allow the more sensitive detection at a time when more of the pyruvate has been converted to lactate (16). We started with the proven method that uses a fixed flip angle in the first scan session and in the second scan session, we then acquired data with both the fixed and variable flip angle scheme in order to compare the two methods. The voxel resolution (2 cm^3) for 2D dynamic acquisition was chosen to replicate the voxel resolution that will be used for the upcoming clinical trial with brain tumor patients. The choice of temporal resolution was based on the balance between the amount of signal observed per image and the total number of time points required for the kinetic modeling. From our experience in previous experiments with rodent models, we selected 3 s temporal resolution as the time resolution for our current study (14,18).

The excellent SNR and spectral quality from the 2D-localized dynamic ^{13}C imaging enabled the assessment of the spatial distribution of metabolites and their evolution over time. A high level of pyruvate and lactate signal was observed throughout the brain and its surrounding tissue. The pyruvate signal peaked shortly after the injection and decreased rapidly from its maximum. When corrected for the variable flip angle scheme, the maximum lactate in the brain appeared ~ 9 s after the maximum pyruvate peak (Fig. 5b), which was consistent with the findings from a previous study using healthy and glioma-bearing rat brains (6).

Differences in estimated metabolic parameters were observed in different regions around the primate brain. Voxels within cerebral hemispheres produced large pyruvate signal, while voxels surrounding the brain appeared to produce relatively low pyruvate signal but exhibited the highest lactate signal (Fig. 4c). The estimated K_{PL} was higher in voxels surrounding the brain compared with voxels within the brain (Fig. 5a). The relatively low SD of K_{PL} across normal brain voxels suggests the robustness of this method to provide a useful baseline for characterizing metabolite kinetics in patients with brain tumors. Similarly, the ratio of lactate to pyruvate was higher in tissue outside the brain (mean \pm SD: 0.30 ± 0.08) compared with the cerebral hemispheres (mean \pm SD: 0.25 ± 0.03) (Fig. 4e). The lactate-to-pyruvate ratio within the primate brain was similar to the one estimated from normal rat brains (6,8). Although the quantification of these metabolic parameters was affected by the relatively coarse spatial resolution causing partial volume effects, they were less sensitive to imaging factors such as polarization, injection time, and volume. The estimated K_{PL} and the ratio of lactate to pyruvate may provide a robust and useful way to quantify in vivo metabolism in both normal and pathologic human brain tissue.

A recent hyperpolarized ^{13}C MR imaging study has investigated the effect of anesthesia level on the cerebral substrate and metabolite signal in rat brain and demonstrated the dependence of cerebral substrate signal levels on isoflurane dose (21). The results from this study may not be directly comparable to a clinical study with brain tumor patients, who will undergo hyperpolarized ^{13}C imaging experiment without anesthesia. The expected level of substrate and metabolite in a clinical study and its comparison with the current study are beyond the scope of this paper.

Future studies will apply the pulse sequences and ^{13}C coils proposed in this study to assess the safety and feasibility of acquiring hyperpolarized ^{13}C metabolic imaging data from patients with brain tumors. In particular, they will seek to confirm the findings from previous preclinical studies using a glioma model (7,20), which demonstrated a significant reduction in ^{13}C metabolism within a few days after treatment, and to investigate the feasibility of this technique as a new imaging tool for detecting early response to therapy in patients with brain cancer.

CONCLUSIONS

We established a hyperpolarized ^{13}C metabolic imaging experimental design that is appropriate for studying patients with brain tumors and demonstrates the feasibility of using hyperpolarized $[1-^{13}\text{C}]$ -pyruvate for assessing in vivo metabolism in a healthy nonhuman

primate brain. Signals from pyruvate and lactate were observed in both the brain and the surrounding tissues. The high SNR of pyruvate and lactate within normal brain indicates that pyruvate is able to cross the blood–brain barrier and provide signals that can be measured using the pulse sequences and coils that we have developed. The kinetics of the metabolite conversion showed that this approach might be useful in characterizing the brain and its surrounding tissues.

Acknowledgments

We gratefully acknowledge the assistance of Bert Jimenez, R.N., and Mary Mcpolin, R.T., for assisting with experiments.

Grant sponsor: National Institutes of Health, Grant numbers: R01EB007588, P41EB13598, R00 EB012064, R21CA170148, R01CA154915, Ilwoo Park was supported by a basic research fellowship from the American Brain Tumor Association.

References

1. Golman K, Zandt RI, Lerche M, Pehrson R, Ardenkjaer-Larsen JH. Metabolic imaging by hyperpolarized ^{13}C magnetic resonance imaging for in vivo tumor diagnosis. *Cancer Res.* 2006; 66:10855–10860. [PubMed: 17108122]
2. Day SE, Kettunen MI, Gallagher FA, Hu DE, Lerche M, Wolber J, Golman K, Ardenkjaer-Larsen JH, Brindle KM. Detecting tumor response to treatment using hyperpolarized ^{13}C magnetic resonance imaging and spectroscopy. *Nat Med.* 2007; 13:1382–1387. [PubMed: 17965722]
3. Albers MJ, Bok R, Chen AP, et al. Hyperpolarized ^{13}C lactate, pyruvate, and alanine: noninvasive biomarkers for prostate cancer detection and grading. *Cancer Res.* 2008; 68:8607–8615. [PubMed: 18922937]
4. Golman K, Petersson JS, Magnusson P, Johansson E, Akeson P, Chai CM, Hansson G, Månsson S. Cardiac metabolism measured noninvasively by hyperpolarized ^{13}C MRI. *Magn Reson Med.* 2008; 59:1005–1013. [PubMed: 18429038]
5. Hu S, Balakrishnan A, Bok RA, Anderton B, Larson PE, Nelson SJ, Kurhanewicz J, Vigneron DB, Goga A. ^{13}C -pyruvate imaging reveals alterations in glycolysis that precede c-Myc-induced tumor formation and regression. *Cell Metab.* 2011; 14:131–142. [PubMed: 21723511]
6. Park I, Larson PE, Zierhut ML, et al. Hyperpolarized ^{13}C magnetic resonance metabolic imaging: application to brain tumors. *Neuro Oncol.* 2010; 12:133–144. [PubMed: 20150380]
7. Park I, Bok R, Ozawa T, Phillips JJ, James CD, Vigneron DB, Ronen SM, Nelson SJ. Detection of early response to temozolomide treatment in brain tumors using hyperpolarized ^{13}C MR metabolic imaging. *J Magn Reson Imaging.* 2011; 33:1284–1290. [PubMed: 21590996]
8. Park I, Hu S, Bok R, et al. Evaluation of heterogeneous metabolic profile in an orthotopic human glioblastoma xenograft model using compressed sensing hyperpolarized 3D (^{13}C) magnetic resonance spectroscopic imaging. *Magn Reson Med.* 2013; 70:33–39. [PubMed: 22851374]
9. Nelson SJ, Kurhanewicz J, Vigneron DB, et al. Metabolic imaging of patients with prostate cancer using hyperpolarized [$1\text{-}^{13}\text{C}$] pyruvate. *Sci Transl Med.* 2013; 5:198ra108.
10. Tropp J, Lupo JM, Chen A, et al. Multi-channel metabolic imaging, with SENSE reconstruction, of hyperpolarized [$1\text{-}(^{13}\text{C})$] pyruvate in a live rat at 3.0 tesla on a clinical MR scanner. *J Magn Reson.* 2011; 208:171–177. [PubMed: 21130012]
11. Tropp, J.; Calderon, P.; Carvajal, L.; Robb, F.; Larson, PE.; Shin, P.; Vigneron, DB.; Nelson, SJ. A carbon receive array of 8 elements, interoperable with proton scanning, for human temporal lobe. Proceedings of the 20th Annual Meeting of ISMRM; Melbourne, Australia. 2012. Abstract 2658
12. Ohliger MA, Larson PE, Bok RA, et al. Combined parallel and partial fourier MR reconstruction for accelerated 8-channel hyperpolarized carbon-13 in vivo magnetic resonance spectroscopic imaging (MRSI). *J Magn Reson Imaging.* 2013; 38:701–713. [PubMed: 23293097]

13. Hu S, Larson PE, Vancracking M, et al. Rapid sequential injections of hyperpolarized [1-(13)C]pyruvate in vivo using a sub-kelvin, multisample DNP polarizer. *Magn Reson Imaging*. 2013; 31:490–496. [PubMed: 23107275]
14. Larson PE, Bok R, Kerr AB, Lustig M, Hu S, Chen AP, Nelson SJ, Pauly JM, Kurhanewicz J, Vigneron DB. Investigation of tumor hyperpolarized [1-¹³C]-pyruvate dynamics using time-resolved multiband RF excitation echo-planar MRSI. *Magn Reson Med*. 2010; 63:582–591. [PubMed: 20187172]
15. Zhao L, Mulkern R, Tseng CH, Williamson D, Patz S, Kraft R, Walsworth RL, Jolesz FA, Albert MS. Gradient-echo imaging considerations for hyperpolarized ¹²⁹Xe MR. *J Magn Reson B*. 1996; 113:179–183.
16. Xing Y, Reed GD, Pauly JM, Kerr AB, Larson PEZ. Optimal variable flip angle schemes for dynamic acquisition of exchanging hyperpolarized substrates. *J Magn Reson*. 2013; 234:75–81. [PubMed: 23845910]
17. Nelson SJ. Analysis of volume MRI and MR spectroscopic imaging data for the evaluation of patients with brain tumors. *Magn Reson Med*. 2001; 46:228–239. [PubMed: 11477625]
18. Zierhut ML, Yen YF, Chen AP, et al. Kinetic modeling of hyperpolarized ¹³C₁-pyruvate metabolism in normal rats and TRAMP mice. *J Magn Reson*. 2010; 202:85–92. [PubMed: 19884027]
19. Ardenkjaer-Larsen JH, Leach AM, Clarke N, Urbahn J, Anderson D, Skloss TW. Dynamic nuclear polarization polarizer for sterile use intent. *NMR Biomed*. 2011; 24:927–932. [PubMed: 21416540]
20. Day SE, Kettunen MI, Cherukuri MK, Mitchell JB, Lizak MJ, Morris HD, Matsumoto S, Koretsky AP, Brindle KM. Detecting response of rat C6 glioma tumors to radiotherapy using hyperpolarized [1-¹³C]pyruvate and ¹³C magnetic resonance spectroscopic imaging. *Magn Reson Med*. 2011; 65:557–563. [PubMed: 21264939]
21. Josan S, Hurd R, Billingsley K, Senadheera L, Park JM, Yen YF, Pfefferbaum A, Spielman D, Mayer D. Effects of isoflurane anesthesia on hyperpolarized (13) C metabolic measurements in rat brain. *Magn Reson Med*. 2013; 70:1117–1124. [PubMed: 23086864]

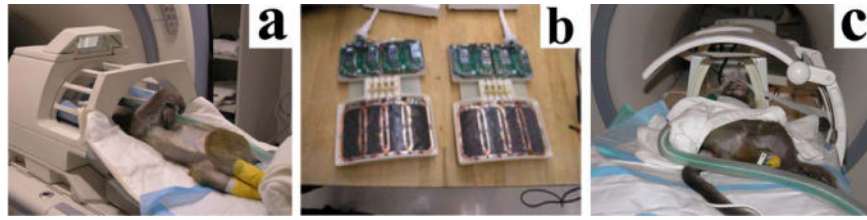


FIG. 1. ^{13}C RF coil configurations developed for human brain studies. **a:** Transmit-receive birdcage volume coil. **b:** Bilateral eight-channel ^{13}C receive coils. **c:** Clamshell volumetric ^{13}C transmit coil and bilateral eight-channel phased array receive coils. [Color figure can be viewed in the online issue, which is available at wileyonlinelibrary.com.]

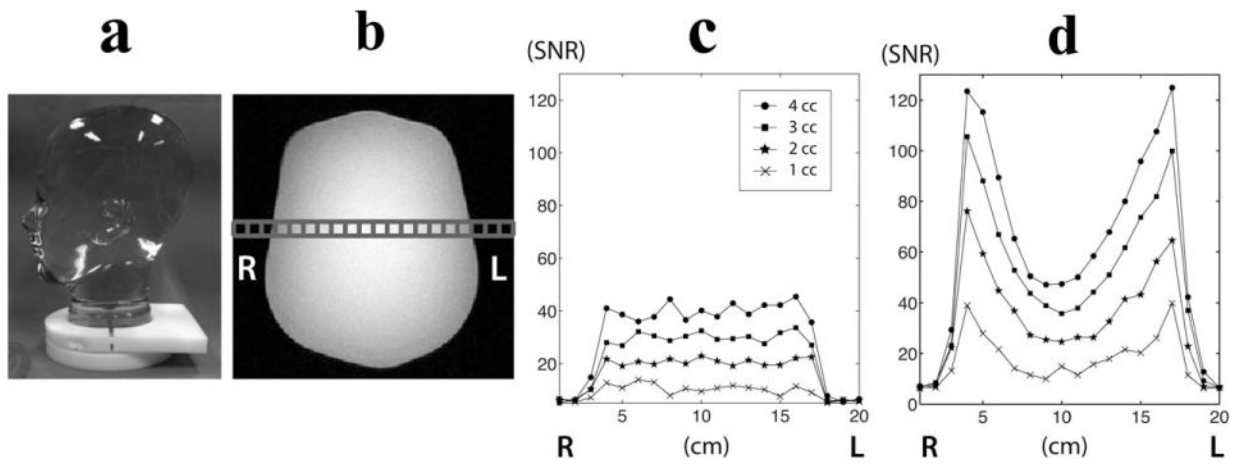
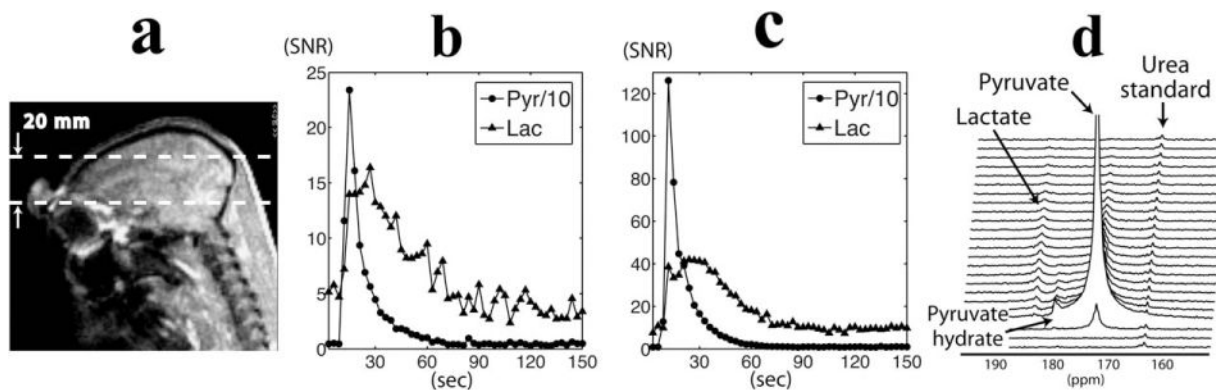


FIG. 2.

A human head-shaped phantom containing ethylene glycol (a) was used for the comparison of SNR between the birdcage (c) and phased array coil (d). A row of spectra in the middle of the phantom (b) was used for SNR comparison.

**FIG. 3.**

Slab-localized dynamic ^{13}C data were acquired from a 20-mm slab through the brain of nonhuman primates (a). The time courses of pyruvate and lactate signal were plotted over time for the data acquired from the birdcage (b) and clamshell/phased array coils (c). The pyruvate signal was scaled by 0.1 for ease of viewing. The stack plot of ^{13}C magnitude spectra from the clamshell/phased array coils shows an uptake of pyruvate and its metabolic products following the injection of hyperpolarized pyruvate (d).

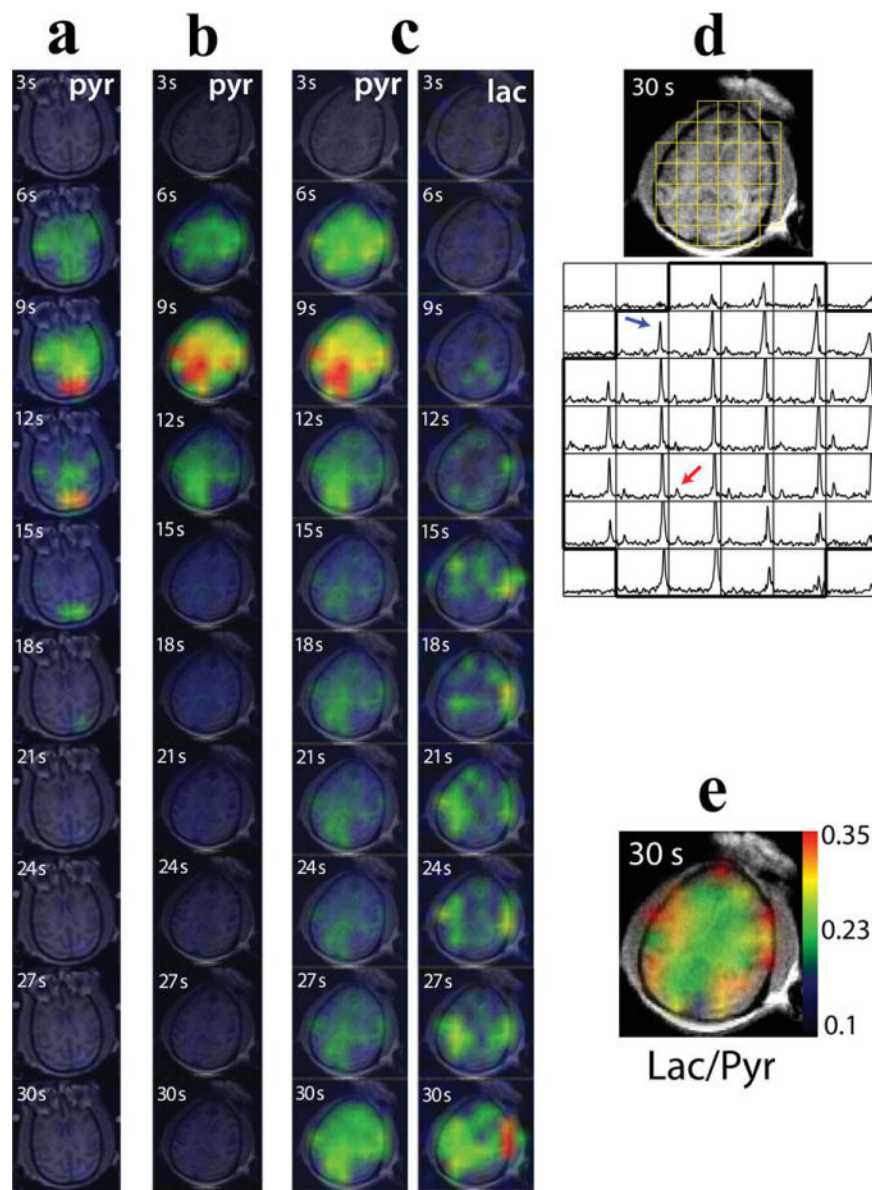


FIG. 4. 2D-localized dynamic ^{13}C spectroscopic data: pyruvate maps acquired with the $20^\circ/4^\circ$ lactate/pyruvate flip angle scheme using the birdcage coil (**a**, examination 1b in Table 1) or the clamshell/phased array coils (**b**, examination 2b in Table 1), pyruvate and lactate maps acquired with the clamshell/phased array coils and variable flip angle scheme (**c**, examination 2c in Table 1), the corresponding ^{13}C spectra (**d**), and the map of the ratio of lactate over pyruvate (**e**) at 30s from the end of pyruvate injection. High pyruvate and lactate signal were observed at the last time point in panel c as a result of the 90° flip angle from the variable flip angle scheme. The red arrow in panel d represents the lactate peak; the blue arrow represents the pyruvate peak. The lactate and pyruvate signal maps were normalized to the corresponding maximum signal.

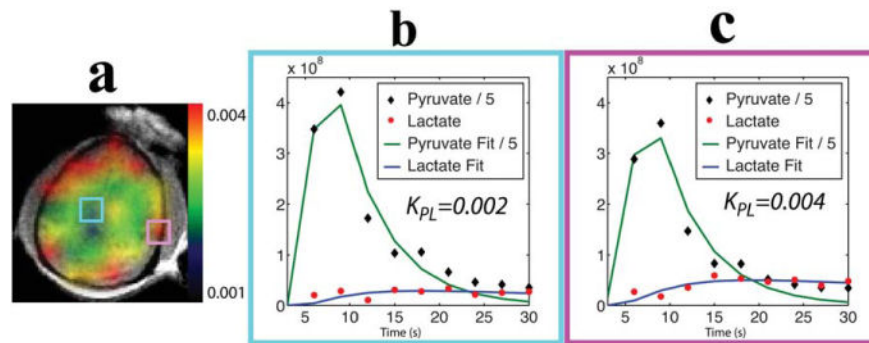


FIG. 5.

a: Map of apparent rate constants for the conversion of pyruvate to lactate from a nonhuman primate brain. Time courses of pyruvate and lactate, which were corrected for the variable flip angle scheme and the corresponding curve fits, are shown for a representative voxel within (b) and surrounding (c) the brain. The pyruvate signal was scaled by 0.2 for ease of viewing.

Table 1

Summary of Nonhuman Primate Studies

Examination	Weight (kg)	Coil Setup	Dynamic Data Type	Polarizer	Pyruvate Injection (mL)	Polarization ^a
1a	4.4	Birdcage	Slice-localized	SpinLab	6.2	10
1b		Birdcage	2D-localized with 20°/4° flip angle for lactate/pyruvate	HyperSense	6.2	23
2a	4.2	Clamshell/phased array	Slice dynamic	SpinLab	5.9	35
2b		Clamshell/phased array	2D-localized with 20°/4° flip angle for lactate/pyruvate	HyperSense	6.4	22
2c		Clamshell/phased array	2D-localized with variable flip angle	SpinLab	5.9	31

The second examination was performed 7 days after the first examination using the same animal.

^aThe liquid state polarization was corrected to the level at the time of pyruvate dissolution assuming a pyruvate T₁ of 60s at 3T.

Table 2

Comparison of SNR Between ^{13}C Birdcage and Clamshell/Phased Array Coils from Ethylene Glycol Head Phantom

Voxel size (cc)	Birdcage ^a	Clamshell/Phased Array ^a	Maximum SNR in Clamshell/Phased Array ^b
1	10.6 ± 0.9	13.1 ± 2.8	39.9
2	20.8 ± 1.6	25.7 ± 0.8	76.2
3	30.4 ± 1.5	39.2 ± 3.6	105.6
4	39.4 ± 2.8	50.8 ± 5.2	124.9

^aSNR was calculated from 4 voxels in the middle. All values are reported as the mean ± SD.

^bMaximum SNR was taken from the row of spectral grid that was used to calculate the mean SNR in 4 voxels in the middle.